

EM-EOF: gap-filling in incomplete SAR displacement time series

Alexandre Hippert-Ferrer ^{*}, *Student Member, IEEE*, Yajing Yan ^{*}, *Member, IEEE*, Philippe Bolon ^{*}, *Member, IEEE*

^{*}LISTIC, Université Savoie Mont-Blanc, Annecy, France
alexandre.hippert-ferrer@univ-smb.fr

Abstract—An iterative method, namely Expectation Maximization-Empirical Orthogonal Functions (EM-EOF) is proposed for the first time to retrieve missing values in SAR displacement time series. This method decomposes the temporal covariance of a displacement measurement time series into different EOF modes by solving the eigenvalue problem, and then selects the optimal number of EOF modes to reconstruct the time series. After an appropriate initialization of missing values, the EM-EOF method performs (i) a cross-validation root-mean-square error (cross-RMSE) minimization to find an estimate of the optimal number of EOF modes used in the reconstruction and (ii) an iterative update of missing values which gives the best estimate of missing data points according to the cross-RMSE. Synthetic simulations have been first performed in order to highlight the efficiency of EM-EOF in the case of various displacement signal complexities and different types of noise and gaps, and a thorough error analysis has been conducted to determine the sensitivity of the method to signal-to-noise ratio (SNR), quantity of gaps and type of noise and gaps. Then, EM-EOF is applied to three displacement measurement time series computed from Sentinel-1 A/B SAR images: two interferograms time series over Gorner and Miage glaciers and one offset time series over the Argentière Glacier covering a period extending from September 2016 to December 2017. Both synthetic simulations and real data applications demonstrate the ability of EM-EOF to retrieve missing values, even in the cases of frequent data gaps, limited size of the time series and spatio-temporally correlated noise and gaps.

Index Terms—gap-filling, EOF, SAR, time series, displacement measurement

I. INTRODUCTION

TIME series analysis of remotely sensed images is an essential tool to better understand some physical phenomena observed on Earth, especially since the recent development of online platforms allowing an easier access to satellite-derived products. From the existing well-developed techniques, differential interferometry (D-InSAR) and offset tracking have experienced continuous improvements over time to compute ground displacement maps from Synthetic Aperture Radar (SAR) images [1]. Regardless of their capability to produce precise ground displacement estimations with enhanced spatial coverage, time series of displacement measurement derived from SAR images can suffer from missing data in both space and time dimensions. Data gaps can occur for various reasons including raw data quality and/or technical limitations of the methods used to compute ground displacements.

Of course, the missing data problem is not new and has been well-documented [2]–[4], especially in optical and infrared

satellite images where data quality is strongly dependent on cloud coverage [5]–[8]. An important framework of gap-filling methods has already been established in ocean-atmosphere, vegetation and hydrology domains [9]–[14]. However, in SAR displacement measurement, existing methods to handle missing data, e.g. regression analysis, nearest-neighbor interpolation (NNI), inverse/angular distance weighting (IDW), spline interpolation and kriging [15]–[18], classically use spatial interpolation of missing values from existing values. Most of these methods include limited temporal information, which can be an issue when dealing with time-evolving physical processes [19]. Moreover, no particular attention has been paid to missing data issues in SAR-derived products such as interferogram and offset time series. On the other hand, complete displacement information can be of particular importance to fully understand the phenomenon under observation, especially for decorrelating targets (e.g. glaciers, vegetated volcanoes, etc.) where data gaps often exist. The main motivation of this paper is to propose a gap-filling method handling both spatial and temporal information of SAR-derived displacement measurement time series.

When filling in gaps in displacement maps computed from SAR images, one has to consider the specificity of the data such as complex displacement behaviors (e.g. linear, oscillatory, etc.), noise correlated at different scales in space and/or time, (e.g. atmospheric perturbations, phase unwrapping errors, etc). Thus, an efficient method aiming at filling in gaps in SAR-derived displacement time series should be able to handle noise and displacement signal complexity. From the existing methods in time series analysis (see [20] and [21] for a review), Empirical Orthogonal Functions (EOFs) have been used to extract spatio-temporal features [9], [22], thanks to their ease of implementation, high efficiency and needless a priori information. EOF analysis is based on the eigenvalue decomposition of the covariance of a time series into orthogonal functions, and allows a representation of the signal into different variability modes such as trends, oscillatory patterns and noise [23], [24]. In InSAR displacement measurement, EOF analysis has recently been used for the first time to extract displacement signal from a time series of Sentinel-1 A/B interferograms over the Gorner glacier [25]. Encouraging results confirm the efficiency of EOF-based methods in the retrieval of spatio-temporal displacement characteristics of time series. Therefore, it seems promising to use the displacement features obtained from EOF analysis to fill in data gaps in InSAR

and offset displacement time series. However, applying EOF analysis directly to time series containing missing values can lead to biases in the sample covariance estimation and thus in the data matrix reconstruction. In order to get around of this issue, the EOF analysis can be combined with the Expectation Maximization (EM) algorithm [26]. The basic idea of the EM algorithm consists of an iterative scheme, with each iteration including 2 steps: the expectation (E) step finds the conditional expectation of missing values given the observed data and current estimated parameters and the maximization (M) step performs maximum likelihood estimation of parameters as if there were no missing data. The EOF analysis can thus be embedded in an EM algorithm with an appropriate initialization of missing values. Given the hypothesis that initialization values are not away from the expected values, an iterative process allows the convergence towards the true values.

Based on this idea, a combination of the EM algorithm and EOF analysis, called EM-EOF, is proposed in this paper. EM-EOF is a data adaptive iterative method to fill in the gaps in SAR displacement time series, and it takes into account the data complexity in terms of both displacement signal and noise behaviors. At E step, the missing values are filled in by expected values. At M step, the temporal covariance of the time series is estimated from the data with data gaps filled in. Then, it is decomposed into EOF modes and a data reconstruction is performed by selecting an optimal number of EOF modes based on a pre-defined criterion. The EM-EOF method proceeds in 2 stages: 1) the first stage consists in finding a first estimation of the optimal number of EOF modes, starting from a relevant initialization of missing values and 2) the second stage is an iterative update of missing values based on the initialization and the optimal number of EOF modes found during the first stage. The final reconstruction is the one that minimizes the distance between the reconstruction and the data used for validation. As ground truth is often not available in displacement measurement by remote sensing, a cross validation technique [27] is proposed to validate the EM-EOF method with available data only. The originality of the present paper lies on the consideration of data gaps in SAR-derived displacement measurement time series and the introduction of the EM-EOF method which takes both spatial and temporal information into account.

This paper is organized as follows : section II describes the EM-EOF method; then, synthetic simulations are presented in section III to demonstrate the ability of EM-EOF to retrieve missing values in time series of various complexity and to analyze the impact of some key parameters such as the initialization value, the quantity of gaps, the type of noise and gaps on the performance of EM-EOF; in section IV, EM-EOF is applied to three displacement measurement time series issued from InSAR and offset tracking of Sentinel-1 A/B images acquired between September 2016 and December 2017 over Gorner, Miage and Argentière glaciers. Finally, conclusions and perspectives are given in section V.

II. THE EM-EOF METHOD

The principle of EM-EOF is summarized in two stages (Fig. 1). The first stage consists in estimating the optimal

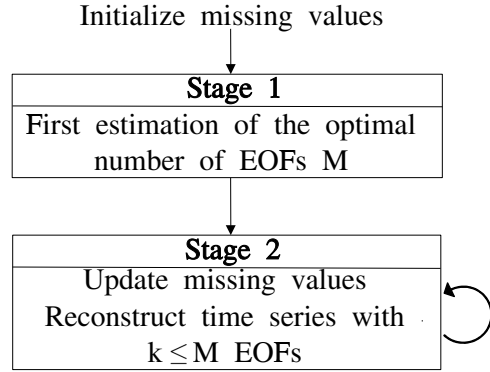


Fig. 1: Diagram of the 2-stages procedure of the EM-EOF method. Data gaps are first initialized with an appropriate value. At stage 1, the optimal number of EOF modes, M , is estimated by minimising an error function. Stage 2 is a refinement stage where updates of missing value are used to reconstruct the time series in an iterative scheme.

number of EOF modes given an appropriate initialization of missing values. For this, the temporal covariance of the time series is decomposed into EOF modes. The appropriate number of EOF modes (denoted by M in the following) to reconstruct the time series is estimated by minimizing the error between validation data and the reconstructed field. The second stage updates the missing values iteratively, based on both previous initialization and optimal number of EOF modes until the algorithm reaches convergence. Details of the EM-EOF method are given in the following.

A. Data organization

Let us suppose that we have a time series represented by a spatio-temporal field $X(s, t)$ which contains the values of the field X at point s and at time t . The values of the field are noted $(x_{st})_{1 \leq s \leq p, 1 \leq t \leq n}$ and may be missing. In matrix form, the field can be written as:

$$X = (\mathbf{x}_1, \mathbf{x}_2, \dots, \mathbf{x}_n) = \begin{pmatrix} x_{11} & x_{12} & \cdots & x_{1n} \\ x_{21} & x_{22} & \cdots & x_{2n} \\ \vdots & \vdots & \ddots & \vdots \\ x_{p1} & x_{p2} & \cdots & x_{pn} \end{pmatrix} \quad (1)$$

where each column $\mathbf{x}_t = (x_{1t}, x_{2t}, \dots, x_{pt})^T$ is an observation over p points at a given time t , and each row is a time series at a given grid point s . An observation \mathbf{x}_t can be an incomplete displacement field, initially represented by a 2-D matrix and reshaped as a column vector of length p . For the computation of the sample temporal covariance (see section II-B), the spatial mean of the field at each time (i.e. mean of each column) is subtracted to form the *spatial anomaly* X' :

$$X' = X - \mathbf{1}_p \bar{X} \quad (2)$$

where $\mathbf{1}_p = (1, \dots, 1)^T$ is a unit vector of length p and $\bar{X} = (\bar{x}_1, \bar{x}_2, \dots, \bar{x}_n)$ is the line vector containing all observation

means with each $\bar{\mathbf{x}}_t$ being the spatial mean of observation \mathbf{x}_t computed as:

$$\bar{\mathbf{x}}_t = \frac{1}{p} \sum_{s=1}^p \mathbf{x}_{st} \quad (3)$$

B. Theoretical background

The sample temporal covariance matrix of X is given by:

$$\hat{C} = \frac{1}{p-1} X'^T X' \quad (4)$$

Note that p can either be equal to the number of all spatial samples or be a subset of samples representing a target or a particular object in the spatial field. In the latter, the data matrix X represents only the target under consideration. The eigenvectors, which are the EOFs of matrix \hat{C} , can simply be found by resolving the eigenvalue equation:

$$\hat{C}U = U\Lambda \quad (5)$$

where U is a $n \times n$ orthogonal matrix and $\Lambda = \text{diag}(\lambda_1, \dots, \lambda_n)$ contains the eigenvalues λ_i of matrix \hat{C} in decreasing order on its diagonal¹. Each column \mathbf{u}_i of U is an eigenvector of \hat{C} and corresponds to each eigenvalue λ_i . U has the property that $U^T U = U U^T = I$, which indicates that each eigenvector is orthogonal to each other.

Since \hat{C} is a symmetric matrix, it follows from the spectral representation theorem that the eigenvalues and the eigenvectors decompose \hat{C} as:

$$\hat{C} = \lambda_1 \mathbf{u}_1 \mathbf{u}_1^T + \lambda_2 \mathbf{u}_2 \mathbf{u}_2^T + \dots + \lambda_n \mathbf{u}_n \mathbf{u}_n^T \quad (6)$$

This decomposition allows a representation of the covariance in terms of EOF modes which describes the temporal variability of the spatial anomaly of the field [24], with each eigenvalue indicating the fraction of total variance explained by the corresponding EOF mode. In general, the first EOF modes represent most of the variability of the signal, which means that most of the behavior of the field X can be explained by just a few leading EOF modes.

X' can be reconstructed by summing the principal components (PCs) a_i multiplied by the eigenvectors:

$$\hat{X}' = \sum_{i=1}^n a_i \mathbf{u}_i^T \quad (7)$$

where the i th PC $a_i = X' \mathbf{u}_i$ is the projection of X' on the i th eigenvector, i.e. a spatial pattern map associated with each eigenvector \mathbf{u}_i . In other words, the PCs refer to the spatial modes of variability of the time series while the eigenvectors show how these spatial modes oscillate with time.

By truncating the summation of (7) at some $M \ll n$, one will keep the EOF modes corresponding to the first (largest) eigenvalues. By doing so, one can extract the main features of the signal because the first EOF modes capture the main temporal dynamical behaviours of the signal whereas other

¹Note that since $U^{-1} = U^T$, equation (5) is equivalent to performing a Singular Value Decomposition (SVD) on matrix \hat{C} and can be noted $\hat{C} = U \Lambda U^T$.

EOF modes represent various perturbations [25]. To decide the number of EOF modes to retain in a given decomposition, it is common to use the measure of the variance contained in the first M EOF modes compared to the total variance of the system given by $f_i = \sum_{i=1}^M \lambda_i / \sum_{i=1}^n \lambda_i$ [9], [24]. A typical choice is to retain those modes that, when summed up, explain 95% of the signal. In case of known data uncertainty, the number of modes to retain can be determined such that the misfits between the reconstruction and the noisy data are, on average, of the order of magnitude of the data uncertainty [28]. [29] also proposed to include data uncertainties into the EOF analysis by computing an error-covariance matrix. To overcome the issue of contamination between neighboring EOF modes/eigenvalues in the case of noisy data, [30] have estimated the eigenvalue uncertainty by a rule of thumb. This can provide useful information when analyzing the eigenvalues, e.g. looking for a discontinuity of the eigenvalues in the spectrum [31]. Moreover, when the statistical characteristics of the noise present in the data are known, a subjective criterion based on Monte Carlo methods can be applied [31], [32], but this implies a priori information on noise characteristics and it is time-consuming. In [25] the difference of squared root-mean-square deviation (RMSD) with respect to noisy data between consecutive number of EOF modes is used to determine the appropriate number of modes to retain, showing that this criterion is consistent with the minimum RMSD with respect to the ground truth.

Despite the existing methods and criteria available in the literature, finding an optimal number of EOF modes remains a challenge, mainly because correlated perturbations are difficult to separate from the displacement signal.

To get the reconstructed field \hat{X} , we finally add the spatial mean back to the anomaly:

$$\hat{X} = \hat{X}' + \mathbf{1}_p \bar{\mathbf{x}} \quad (8)$$

In the case where a spatial field is composed of multiple objects each with a different temporal behavior, the reconstruction of the spatial field can be performed object by object. The sample temporal covariance should be estimated using only spatial samples related to each object and the reconstruction of the spatial field is obtained from the mosaic of the reconstructions of each object.

C. Initialization of missing values

Initialization of the missing values constitutes a key parameter of the EM-EOF method because it impacts the estimation of the temporal covariance matrix \hat{C} and thus the computation of the EOFs. In fact, the covariance matrix can be estimated using only available values [33], [34], but this does not always lead to a positive semi-definite covariance matrix [9]. As the initialization value is considered as a first estimate of the missing values, it is clear that it should be set in accordance to the distribution of the observed values. This assumption indicates that such an initialization should perturb as little as possible the variance distribution of different modes composing the displacement field. To avoid any bias in the anomaly matrix, data gaps can be initialized by the spatial mean (corresponding

to zero in the anomaly) [11], [35]. However, [9] have shown that an initial filling of missing values by the spatial mean tends to diminish the variance of higher order modes by inversely increasing the variance of the dominant modes. Such an initial value tends to erase small scale information because it smooths the displacement field around missing data points. As no thorough study has been performed to compare different initialization values and to investigate their impact on the efficiency of the EOF analysis, a discussion focused on the impact of the initialization value on the performance of the EM-EOF method is given in section III-E. In the following, we denote by $\mathbf{x} = (x_{st}^0, x_{st}^1, \dots, x_{st}^m) \subseteq X$ the set of missing data points of matrix X embedded in a m -length vector \mathbf{x} .

D. Cross-validation

In order to assess the reconstruction error and to select the optimal number of EOF modes, a cross-validation root-mean-square error (cross-RMSE) is proposed [27]:

$$E(k) = \left[\frac{1}{N} \sum_{i=1}^N |\hat{\mathcal{X}}_k - \mathcal{X}|^2 \right]^{1/2} \quad (9)$$

where $\mathcal{X} = \{x_i\}_{1 \leq i \leq N}$ is the cross validation data subset of X which contains N points randomly chosen in space and time among existing data. These points are set as artificial missing data with their values set aside. After each reconstruction with k EOF modes, the cross validation data set \mathcal{X} is compared to the new estimated set $\hat{\mathcal{X}}_k$. The number of points N must be neither too small nor too large: a small N will not provide a good statistical representation of the data whereas a large N can affect the reconstruction error since the quantity of missing data is increased. Cross-RMSE is particularly useful when no ground truth or other source of information is available for validation of the results, which is often the case in displacement measurement.

E. Stage 1: find a first estimation of the optimal number of EOF modes

Stage 1 is described by the pseudo-code in Algorithm 1. After the initialization of missing values, we perform the computation of (4) and (5) and reconstruct the time series anomaly as in (7) by successively adding one EOF mode at a time. The reconstruction of the time series with k EOF modes is noted \hat{X}_k , which gives new estimated values $\hat{\mathbf{x}}$ of the missing data points \mathbf{x} , with the observed values remaining unchanged. Every time an EOF mode is added, we compute $E(k)$. The optimal number M is then found as the number which minimizes the cross-RMSE:

$$M = \arg \min_{M \in [1, n]} E(k) \quad (10)$$

where $k = 1, \dots, n$ and n is the maximum number of EOF modes (i.e. the time dimension here).

Algorithm 1 Stage 1: find first estimation

Input: X , init_value
Output: M

- 1: $\hat{\mathbf{x}} \leftarrow \text{init_value}$
- 2: **for** $k \leftarrow 1, n$ **do**
- 3: Compute (4), (5) to find \hat{C}, U
- 4: Compute (7) with k EOF modes to obtain $\hat{\mathbf{x}} \subseteq \hat{X}_k$
- 5: Compute $E(k)$
- 6: **end for**
- 7: **return** $\arg \min_{M \in [1, n]} E(k)$

F. Stage 2: update missing values

Stage 2 is described by the pseudo-code in Algorithm 2. It is a refinement stage: for each number of EOF mode k , (4), (5) and (7) are computed in an iterative loop. At iteration i , the reconstruction is performed using the new values of the missing data obtained at the last iteration. The cross-RMSE is computed at each iteration. The convergence is obtained only if the difference $\Delta E = E_i(k) - E_{i-1}(k)$, where $E_i(k)$ denotes the cross-RMSE at iteration i with k EOF modes, is smaller than a predefined convergence value α . A small value, generally close to 0, is appropriate for α . Once the convergence is met, one more EOF mode is added to the reconstruction and the iteration process starts again with $k+1$ EOF modes. If the cross-RMSE starts to increase, the procedure stops, otherwise it keeps going until the number of EOF modes M is reached. Note that the optimal number M of EOF modes estimated at stage 1 might not be reached during stage 2, which essentially depends on SNR and the quantity of missing data. During iterations, the update of missing data points tends to smooth the displacement field (hence the term refinement used here). In other words, a refined reconstruction with k EOF modes might give a better estimation at the missing points than a reconstruction with $k+1$ EOF modes with no refinement.

In the case of a displacement signal perturbed by strong correlated noise, the optimal number of EOF modes can be over-estimated. To deal with this issue, we look at the quantity $1 - E(k+1)/E(k)$, which gives a measure of the variation of the cross-RMSE when adding one more EOF mode. A small variation (for example less than a value β) implies that only little information is added to the new reconstructed field: in this case, the added EOF mode is not taken into account in the reconstruction. If the data uncertainty is known, β can be determined such that the reconstruction uncertainty is consistent with the data uncertainty. If the uncertainty is unknown, β is determined empirically. In most cases, a value of 0.1 (which means that if the variation of the cross-RMSE when adding one EOF mode falls below 10% of $E(k)$, the algorithm is stopped) is sufficient to select an optimal number of EOF modes. At the end of stage 2, the time series is reconstructed with the estimated number of EOF modes using (7).

III. SYNTHETIC SIMULATIONS

The goal of this study is (i) to demonstrate the ability of the EM-EOF method to retrieve missing values in various

Algorithm 2 Stage 2: update missing values

Input: X, M, α, β
Output: \hat{X}_k

```

1: for  $k \leftarrow 1, M$  do
2:   while  $|\Delta E| < \alpha$  do
3:     Compute (4), (5), (7) to find  $\hat{C}, U, \hat{x} \subseteq \hat{X}_k$ 
4:      $\hat{x} \leftarrow \hat{x}$ 
5:     Compute  $E(k)$ 
6:   end while
7:   if  $E(k) > E(k-1)$  or  $1 - E(k)/E(k-1) < \beta$  then
8:     return  $\hat{X}_{k-1}$ 
9:   end if
10: end for
11: return  $\hat{X}_k$ 

```

displacement time series of different complexities and (ii) to highlight the impact of key parameters such as the type of noise, the type of gaps, the initialization value of missing data on the quality of the reconstruction.

A. Type of displacement

To simulate the displacement time series, displacement models with different complexity are generated (Table I), starting from a first order field g_1 formed using a linear function to n -order ($2, 3, 4, \geq 4$) fields g_2, g_3, g_4 and g_6 formed with sums of sines and cosines to reproduce an oscillatory displacement with multiple frequencies. A fifth synthetic field g_5 representing an exponential decaying post-seismic displacement is also generated using the Pyrocko toolbox [36].

	$g(r, t)$	Order
g_1	$(1 - 0.5r_1)t$	1
g_2	$g_1 + \sin(2\pi f_1 t) \cos(2\pi f_1 r_1)$	2
g_3	$g_2 + 0.5 \cos(2\pi f_2 t) \cos(2\pi f_3 r_1)$	3
g_4	$g_3 + 0.1 \sin(2\pi f_4 t) \cos(2\pi f_5 r_1)$	4
g_5	$A - b \exp(-t/\tau_e) + 10^{-4}t$	-
g_6	$g_1(r_1) + g_3(r_2) + g_3(r_3) + g_4(r_1)$	≥ 4

TABLE I: Deterministic fields used in synthetic simulations. g_1 is linear in space and time dimension whereas g_2, g_3 and g_4 include oscillations of different frequencies with a linear basis. g_5 is a post-seismic deformation with decaying time $\tau_e = 1.5$, and constants $A = 0$ and $b = 1$. $r_1 = \sqrt{x^2 + y^2}$, $r_2 = \sqrt{(x-1)^2 + (y-1)^2}$ and $r_3 = \exp(-(x+y)^2) + xy + \tan(x)$ are the distances from the origin with coordinates (x, y) varying in the compact interval $[-1, 1]^2$ and t is the time of observation. Values of the frequencies are : $f_1 = 0.25, f_2 = 0.75, f_3 = 2.5, f_4 = 1.25, f_5 = 5$.

B. Type of noise

SAR-derived displacement measurements are subject to perturbations of diverse origins. To be representative of the different natures of perturbations, we simulate: 1) a spatially

correlated noise, 2) a spatio-temporally correlated noise and 3) a noise-like phase unwrapping error. Spatial and temporal noise correlations are driven by two correlation coefficient $\gamma, \rho \geq 0$, whereas unwrapping errors are simulated by artificial jumps of the displacement values (phase jumps). Details of the generation of the first two types of noise are presented in Appendix A.

C. Type of gaps

Due to various origins, data gaps can be randomly distributed in space and/or in time, or their distributions can be spatially and/or temporally correlated. For example, spatially correlated data gaps are often observed in offset measurements over glaciers due to snow falls or rapid glacier flow or in InSAR measurements over vegetation areas due to seasonal coherence loss. Here, we consider two types of data gaps: 1) gaps randomly distributed in space and time and 2) gaps which have an evolving shape in space and time. In the latter case, gaps are only generated on eight consecutive displacement maps to simulate data gaps related to a seasonal event (winter snow falls, vegetation in summer, etc.).

D. Experiments setup

6 time series of 40 displacement maps are generated, 5 of which include only one type of displacement field (one target) each corresponding to g_1, \dots, g_5 . The 6th time series g_6 corresponds to a simulation of multiple targets with different spatio-temporal behaviors. The spatial dimension for g_1 to g_4 is 200×200 and 4000×4000 for g_5 and g_6 . All displacement time series are perturbed by both random and correlated gaps, as well as spatially and spatio-temporally correlated noise. The amount of gaps varies from 0 to 80% and the signal-to-noise ratio (SNR) varies between 0.5 and 4.5 to test the impact of both parameters. To compare the effect of initialization on the final reconstruction, initial filling is performed with three values: 1) the spatial mean of the data, 2) the spatial mean plus spatially correlated noise which has the same correlation coefficient γ ($\gamma = 1.1$) and the same distribution as the noise present in the data and 3) the spatial mean plus random noise following a Gaussian distribution. Main experiments setups (with results presented in the following section) are summarized in Table II.

E. Results and discussions

a) *Comparison of different initialization values:* repeated experiments with initial values taken from spatial mean plus a random noise following a Gaussian distribution and spatial mean plus a spatially correlated noise have been performed. They show no difference in both the final cross-RMSE and the optimal number of EOF modes compared to the initialization with the spatial mean. However, it is observed that the time of convergence of the iterative update at stage 2 can be considerably increased with an initial filling with the spatial mean plus random or correlated noise. We therefore choose to initialize missing data points by the spatial mean in all the experiments since 1) it avoids any bias in the reconstruction

Case	Order	Type of gaps	Type of noise	SNR
1	1	Random	Spatially corr.	1.44
		Spatially corr.	Spatio-temporally corr.	1.47
	2	Random	Spatially corr.	1.45
		Spatially corr.	Spatio-temporally corr.	1.24
2	3	Random	Spatially corr.	1.61
		Spatially corr.	Spatio-temporally corr.	1.43
	4	Random	Spatially corr.	1.46
		Spatially corr.	Spatio-temporally corr.	1.24
	-	Random	Spatially corr.	1.7
3	multi	Random	Spatially corr.	1.4
		Corr.	Spatio-temporally corr.	1.4

TABLE II: Experiments setups of case 1, case 2 and case 3 with 30% of gaps and an initialization by the spatial mean. "Corr." refers to correlated. To test the impact of SNR and the quantity of gaps, more experiments are drawn with SNR values from 0.5 to 4.5 and gap quantities from 0% to 80%. In these cases, three values of initialization are tested: spatial mean, spatial mean plus random noise and spatial mean plus spatially correlated noise to highlight the impact of initialization on the reconstruction.

and 2) it does not require knowledge on the noise present in the data.

Results of the reconstruction of the first and second order fields g_1 and g_2 are presented in Fig. 2 (Case 1). Fig. 4 illustrates the results of the third (g_3), fourth order (g_4) and post-seismic displacement fields (g_5) (Case 2). Fig. 5 shows time series associated with the fields of cases 1 and 2. Finally, Fig. 7 shows the results for the multi-target displacement field (g_6) (Case 3).

b) *Case 1 - first and second order fields:* in this case, the optimal number of EOF modes is estimated to be 1 for the first order field and 2 for the second order field. The reconstructed fields show a displacement pattern in good agreement with the true field, without degradation by the missing data in both cases of random (Fig. 2 (a)(c)) and correlated (Fig. 2 (b)(d)) gaps, which is also confirmed by the similarity between residuals and noise. The reconstructed field is however more affected by spatio-temporally correlated noise, part of which can still be observed in the reconstruction. Fig. 5 (a)(b) shows the initial and reconstructed time series of some spatial points in the second order field case. This result shows that the EM-EOF method is able to reconstruct temporal evolution trends which suggests, together with results in Fig. 2, its capacity to interpolate in both space and time dimensions. Fig. 2 (d) and Fig. 5 (a) also show the reconstruction result with unwrapping errors. New estimated values at the phase jumps location are in accordance with the overall displacement field, and residuals indicate that phase jumps are filtered out by the EM-EOF method, which is mainly explained by the fact that such high frequency events are represented in higher EOFs modes. Cross-RMSE in function of gaps percentages and SNR in the cases of the first and second order displacement fields perturbed by spatio-temporally correlated noise are shown in

Fig. 3. It is observed that the reconstruction performance is mainly affected by SNR compared to the quantity of gaps, except for large quantities ($> 60\%$) of random gaps (Fig. 3 (a)(c)). Note that random gaps affect more the reconstruction quality than correlated gaps (Fig. 3 (b)(d)) because gaps are only simulated over ten consecutive displacement maps in the latter. Actually, a large quantity of random gaps also means a larger probability that a data point might be missing over n consecutive displacement maps. If we call \mathcal{P} this probability, it can be computed as $\mathcal{P} = (q/100)^n$ where q is the percentage of data gaps. With $n = 40$, \mathcal{P} is almost negligible for $q < 60\%$, which is consistent with the observed smaller cross-RMSE.

c) *Case 2 - third, fourth order fields and post-seismic deformation:* in this case, the optimal number of EOF modes is 3 for the third order field, 5 for the fourth order field and 2 for the post-seismic field (Fig. 4). In all cases, a global agreement is observed between the reconstructed and true fields in both space and time, even in the presence of phase unwrapping errors perturbations as shown in Fig. 5 (c)(d). In the case of the fourth order field, a part of the displacement signal is observed in the residual, but the amplitude remains small, and the reconstructed field still contains noise. As a matter of fact, the choice of the optimal number of EOF modes is more challenging when complex displacement signal is perturbed by noise, especially when the SNR is low and when displacement and noise behaviours are similar. Here, strong spatio-temporally correlated noise perturbing the field can lead to an over-estimation of the number of EOF modes, which is mainly explained by the fact that both noise and displacement signal are correlated in space and time, which makes them difficult to separate. In this case, parameter β (see section II-F) can be increased to avoid the over-estimation. Error maps of the third and fourth displacements fields in function of SNR and quantity of gaps show that large quantities of gaps affect more the reconstruction in the case of randomly distributed gaps (Fig. 6 (a)(c)), particularly when the displacement is more complex as in the case of a fourth order field (Fig. 6 (c)). With 30% of data gaps, the quality of the reconstruction only depends on the SNR in all cases. In the case of the post-seismic deformation, Fig. 6 (e)(f) shows that the method is slightly less sensitive to large quantities of random gaps compared to correlated gaps.

d) *Case 3 - multiple pattern fields:* each displacement field is composed of a linear displacement field g_1 , two third order fields g_3 and one fourth order field g_4 . First, one reconstruction of the whole spatial field is performed. The missing values are initialized by the spatial mean. The optimal number of EOF modes is 4 for a field perturbed by both random gaps and spatially correlated noise (Fig. 7 (a)) and 6 for a field perturbed by correlated gaps and spatio-temporally correlated noise (Fig. 7 (b)). In both cases, the reconstruction shows satisfactory patterns compared to the true field. Transitions between patterns are preserved even in the case of correlated gaps which extend across all spatial patterns, but residuals still show a small part of the fourth order displacement. In the case of correlated gaps, the linear field is slightly over-reconstructed, that is a part of the perturbing noise is also

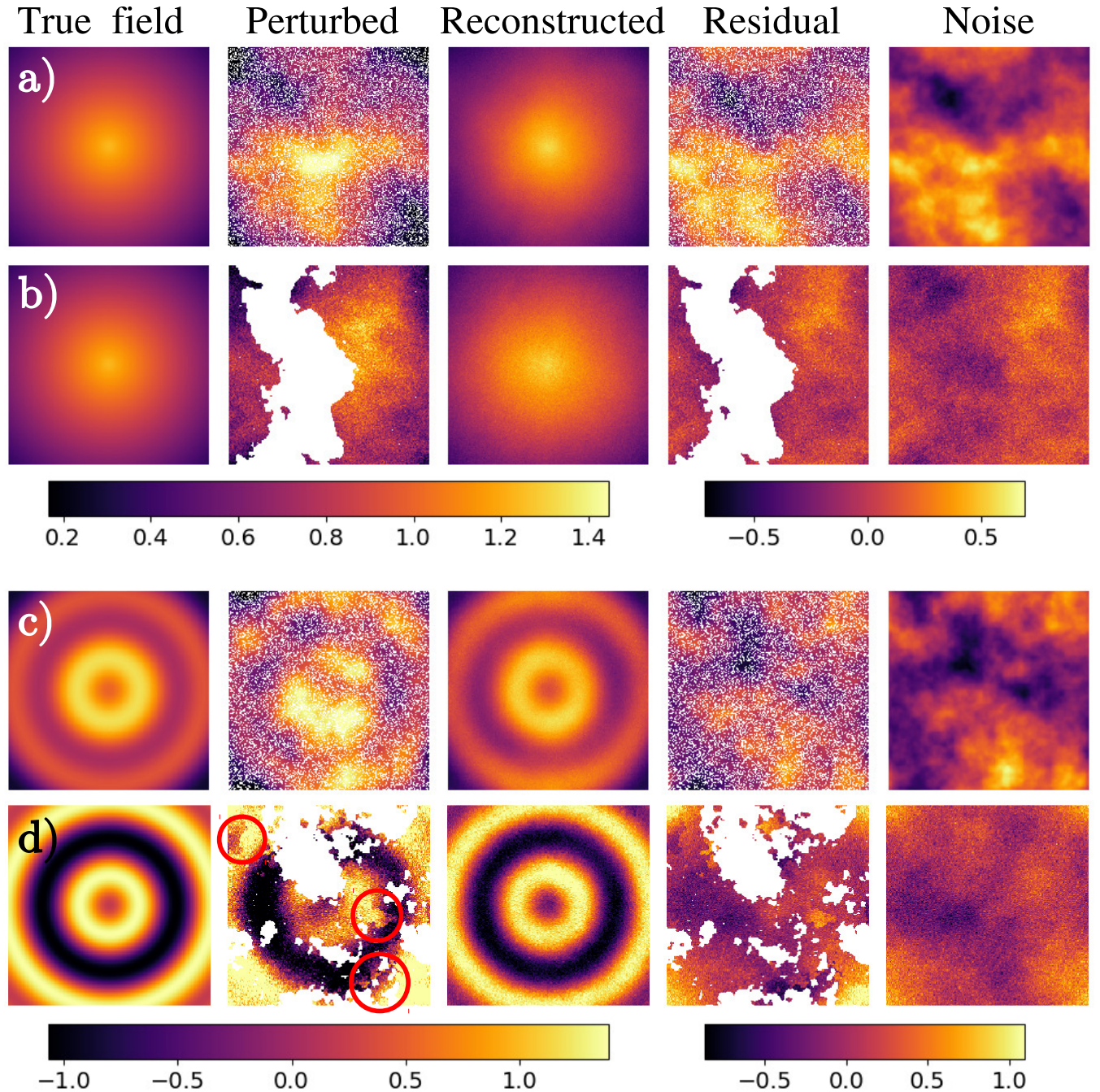


Fig. 2: Result of the reconstruction of displacement fields [cm] of (a) (b) first order and (c) (d) second order containing 30% of missing data and with $1.24 \geq \text{SNR} \geq 1.44$. Displacement fields are perturbed by (a) (c) random gaps and spatially correlated noise, and (b) (d) correlated gaps and spatio-temporally correlated noise. In (d), unwrapping errors are simulated as phase jumps (red circles). The residual is the difference between the reconstructed field and the perturbed field.

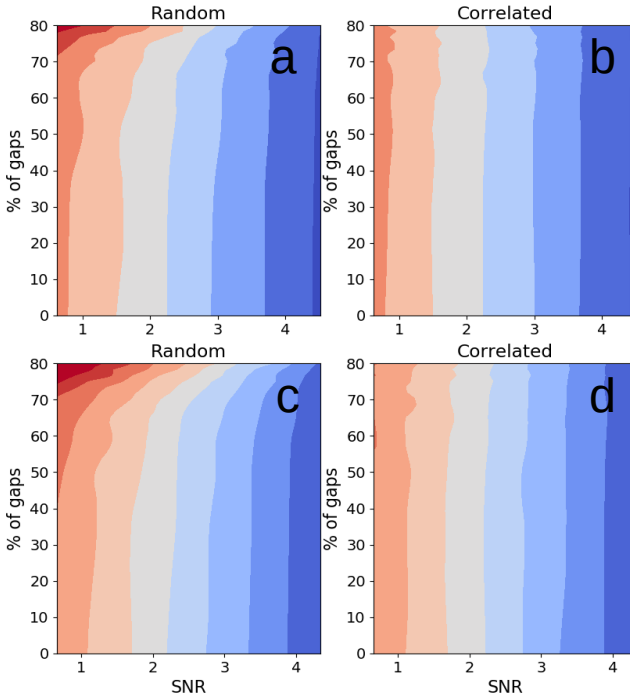


Fig. 3: Cross-RMSE [cm] as a function of % gaps and SNR in case of a first order displacement time series with (a) random gaps and (b) correlated gaps, and a second order displacement time series with (c) random gaps and (d) correlated gaps. All displacement time series are perturbed by spatio-temporally correlated noise.

reconstructed. For comparison, 4 independent reconstructions for each displacement pattern with different optimal number of EOF modes have also been performed. The results are shown in Fig. 8. In the reconstructed field, the displacement characteristics of each pattern are more preserved. The improvement of this multi-reconstruction strategy is highlighted in case of the fourth order displacement, where all fringes are now reconstructed. Indeed, when the discontinuities between displacement patterns are relatively sharp, it is preferred to perform the reconstructions separately, particularly in case where displacement patterns are very different from one to another, which implies different number of optimal EOF modes for the reconstruction. When transition zones cannot be clearly identified (as in most cases of ground displacement fields), one reconstruction of the whole field is recommended to avoid possible discontinuities between displacement patterns.

To summarize, the reconstruction quality is more dependent on the SNR than the quantity of gaps. However, the reconstruction quality is driven by both SNR and the quantity of gaps if gaps are randomly distributed ($> 60\%$). In the case of complex displacement behaviour, larger cross-RMSE are obtained and the EM-EOF method is more sensitive to spatio-temporally correlated noise than spatially correlated noise: in the former case, the problem of over-estimation of the optimal number of EOF modes is observed. In case of displacement patterns with different temporal behaviors, the strategy of multiple reconstruction can be considered depending on the difference

of displacement behavior between patterns and on the number of patterns under consideration.

F. Computational burden

As EM-EOF works on temporal covariances, it is rather the temporal dimension than the spatial dimension that limits its application. It can deal with pluriannual time series of large displacement maps without difficulty. To give an example of the computational burden of the method, we present mean run times in Table III using an Intel Xeon E5-2650 v3 at 2.3GHz, which is a standard processor used in regular stations.

Image size (pixels)	Distance in Sentinel-1 data (km)	Run time (s)
100×100	0.35×2.2	0.07
1000×1000	3.5×22.2	17.1
2000×2000	7×44.4	82.4 (1 min 22.4 s)
4000×4000	14×88.8	295.5 (4 min 55.5 s)
5000×5000	17.5×111	499 (8 min 19 s)

TABLE III: Mean computational run times of the EM-EOF algorithm for time series of 40 synthetic images with 30% of missing data.

G. Comparison with other interpolation methods

To evaluate the performance of the EM-EOF method along with other interpolation methods, a comparison based on the cross-RMSE (Fig. 9) has been conducted with Nearest Neighbor Interpolation (NNI) [37] and Kriging [38]. Note that because the library used for Kriging requires longer computational time, the experiment has been conducted on a time series of small synthetic images of size 50×50 . In all cases, EM-EOF shows better performance than NNI and Kriging, especially in the case of low SNR where the gain is larger. Kriging is also less sensitive to large quantities of random gaps than EM-EOF and NNI (Fig. 9 (a)) since it is based on semivariance instead of geometrical distance [39] (as it is the case of NNI). The surge of EM-EOF cross-RMSE is due to the increasing unavailability of temporal points in the time series. In the case of correlated gaps (Fig. 9 (b)), Kriging performance is close to that of EM-EOF whereas NNI performs inefficiently.

IV. APPLICATION TO DISPLACEMENT TIME SERIES OF ALPINE GLACIERS

EM-EOF is applied separately to three displacement measurement time series obtained from a time series of Sentinel-1 A/B SAR images: two time series of 6-day interferograms over Gorner and Miage glaciers and one 12-day offset time series over the Argentière Glacier (Fig. 10). Displacement maps, as well as time series at chosen locations over glaciers are presented in this section. Since the displacement fields under consideration are relatively homogeneous, only one covariance decomposition and one EOF reconstruction are performed for each glacier. All data sets contain missing data because of

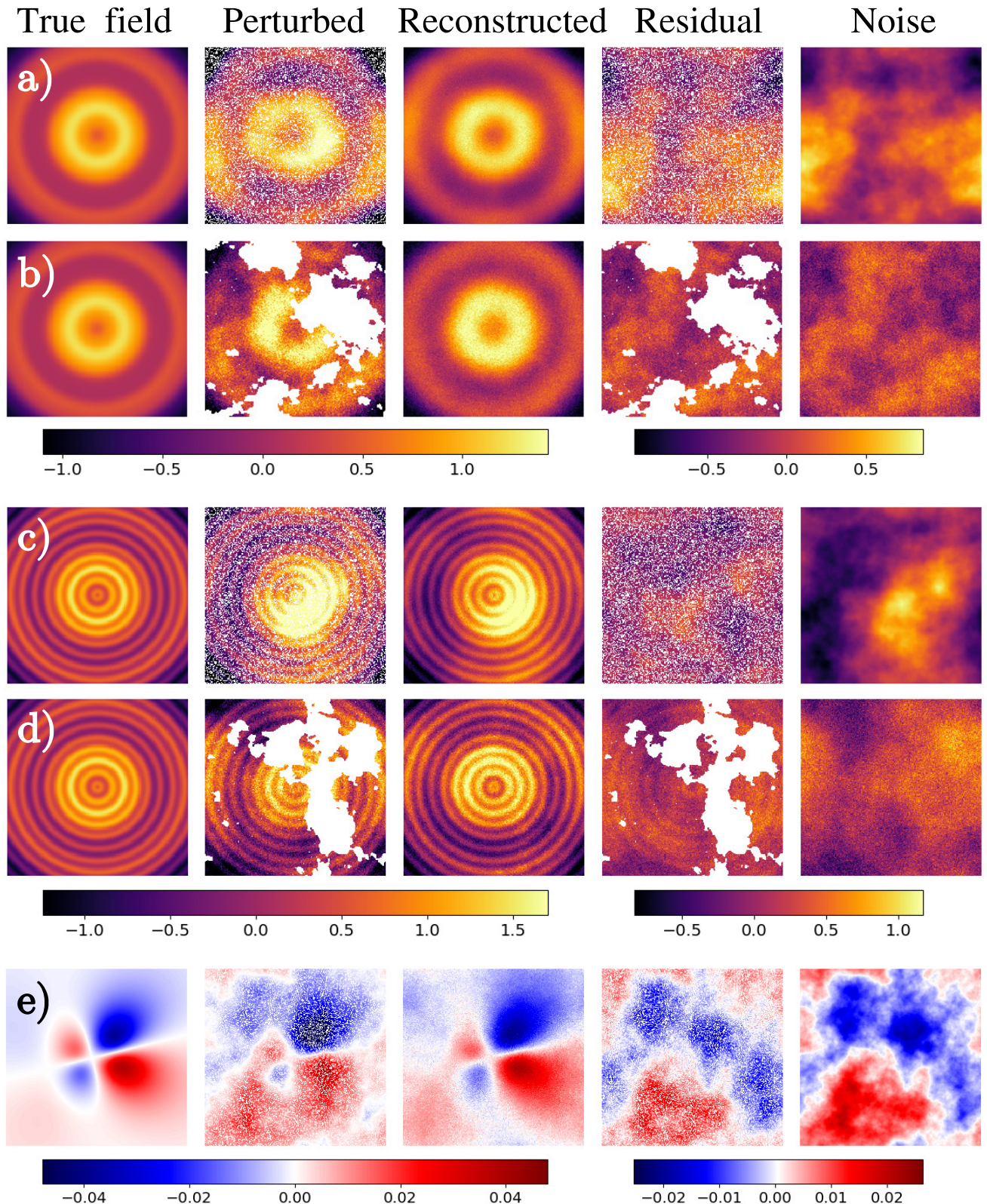


Fig. 4: Result of the reconstruction [cm] of (a) (b) third order, (c) (d) fourth order, and (e) post-seismic displacement fields containing 30% of missing data and with $1.24 \geq \text{SNR} \geq 1.61$. Displacement fields are perturbed by (a) (c) (e) random gaps and spatially correlated noise, and (b) (d) correlated gaps and spatio-temporally correlated noise. The residual is the difference between the reconstructed field and the perturbed field.

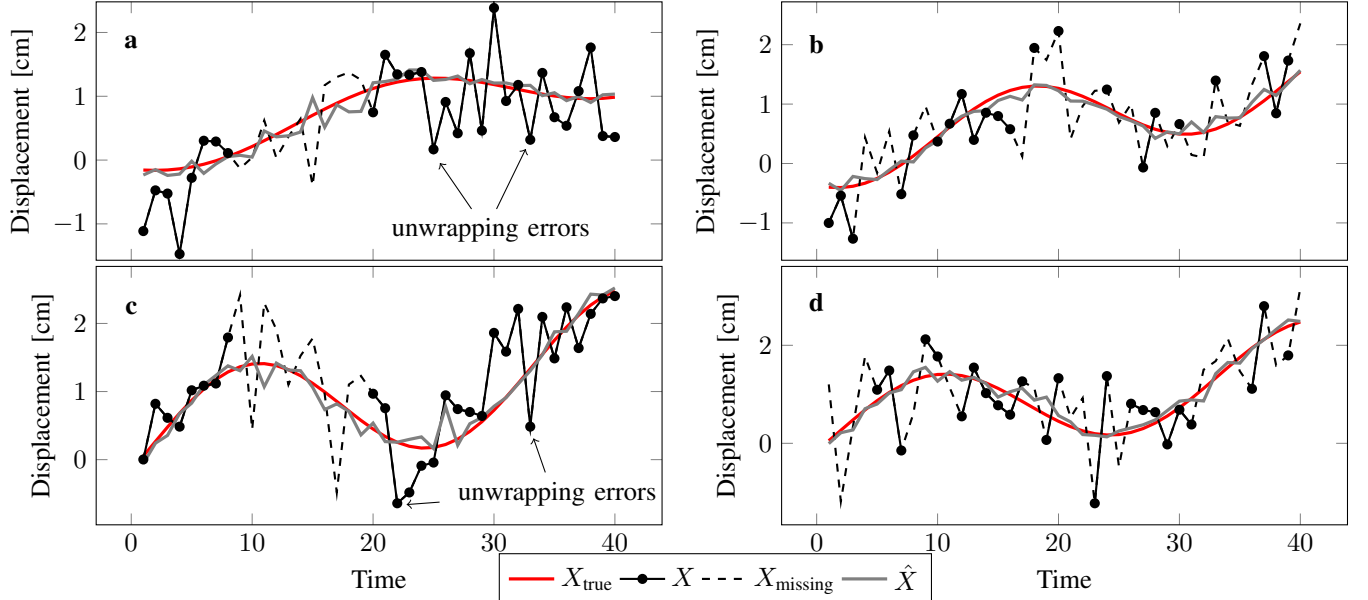


Fig. 5: Displacement time series of arbitrarily chosen points over (a)(b) a second order field and (c)(d) a third order field. (a)(c) show results with correlated missing data on 10 consecutive dates and (b)(d) with random missing data (50%). Red line denotes the true displacement, black circle indicates the perturbed displacement with noise and gaps, black dotted line is the missing data and gray line is the reconstructed time series. SNR varies from 1.5 to 2.

fast glacier flow and/or snow falls during some acquisitions. Missing values are initialized by the spatial mean. We choose to set the number of cross-validation points (randomly chosen) to 1% of the observed points per displacement map.

A. Gorner Glacier

16 interferograms were computed from consecutive Sentinel-1 A/B acquisitions between November 2016 and March 2017. Data gaps are spatially correlated, with quantities per interferogram varying from 11.8 to 27.4 %. The time series also contains four missing interferograms. The quality varies from one interferogram to another, with 12 (out of 16) interferograms being of good quality according to the coherence.

The optimal number of EOF modes to reconstruct the time series is estimated to be 3. Representative examples of the reconstruction are presented in Fig. 11 : case 1 (first row) contains 14.6% of data gaps, case 2 (second row) is one missing interferogram (100% of data gaps) and case 3 (third row) contains 27.4% of data gaps.

In case 1, the reconstructed displacement signal shows consistent patterns in missing data areas with the overall displacement field, with a smoother texture in observed areas compared to the original interferogram, i.e. the reconstruction does not degrade the displacement pattern. No clear displacement signal is observed in the residual and the major part of the glacier also shows relatively homogeneous and small zero-centered residuals. Large residuals are observed close to the left glacier edges where localized phase unwrapping errors exist due to abrupt transition between static rock and ice in motion, as well as discontinuities due to coherence loss. Results on time series at locations P₁, P₂ and P₃ (see

Fig. 11) show that the reconstructions fit the observed values even with abrupt fluctuations as in mid-November 2016 and mid-February 2017 (Fig. 12 (a)). Reconstruction at location P₂, where few observations exist, can be validated by the nearby location P₁ which is substantially more observed than P₂. Note that slight difference is observed between some observed values and reconstructed values, which is due here to the noise filtering property of the EOFs. To reconstruct the missing interferogram (case 2), the temporal mean (instead of the spatial mean which cannot be computed) is added to the reconstructed anomaly. The reconstructed displacement pattern is consistent with those observed on other interferograms in the time series and also with those obtained in [25]. The reconstruction of case 3 also shows a consistent displacement pattern with the initial field. On the original interferogram, data gaps (due to low coherence) induced phase unwrapping errors in some localized area, which results in discontinuities of displacement values in the residuals, where large values are mainly observed. However, no displacement signal can be identified in the residual. The means and standard deviations of residuals on observed and cross-validation points for all interferograms are shown in Table IV. The means of residuals are small: less than 0.05 cm on observed points and less than 0.2 cm on cross-validation points for most interferograms. On one hand, this is consistent with the observations in Fig. 11 that the EM-EOF method does not degrade the observed points of good quality. On the other hand, this confirms the capability of the EM-EOF method to fill in data gaps with accuracy. Slightly larger values for cross-validation points are mainly explained by the fact that it represents only a small part of the total observed points (1%). Moreover, the consistency between the observed and cross-validation values confirms

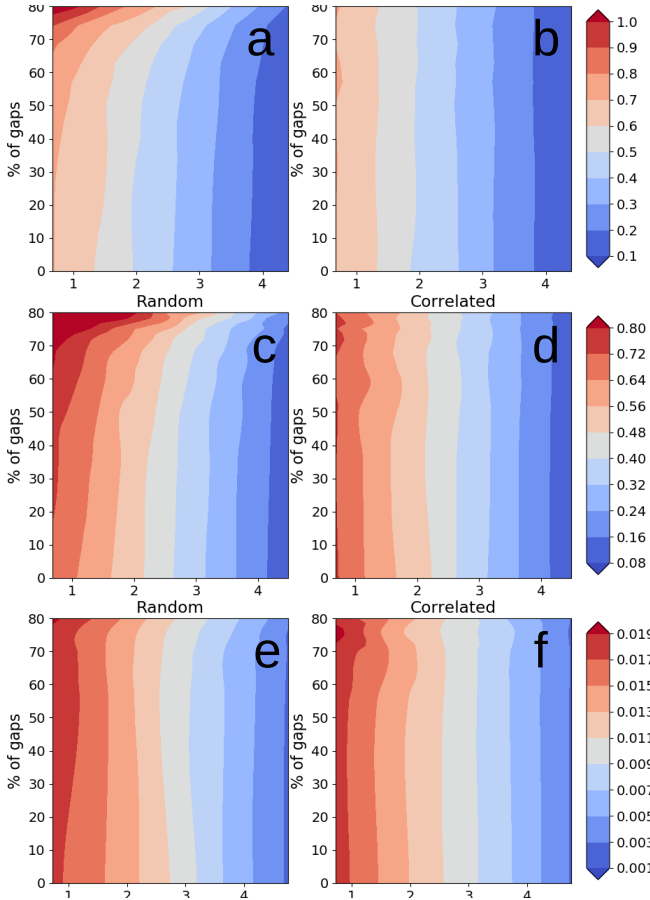


Fig. 6: Cross-RMSE [cm] as a function of % gaps and SNR in case of a third order displacement time series (a)(b), fourth order displacement time series (c)(d) and post-seismic deformation (e)(f). First column are field perturbed by random gaps, second column by correlated gaps. All displacement time series are perturbed by spatio-temporally correlated noise.

the robustness of the selected cross-validation data. Most standard deviation values are smaller than 1 cm on observed points and 1.8 cm on cross-validation points. Larger standard deviations for observed points on some interferograms are mainly explained by localized phase unwrapping errors in the original interferograms. For cross-validation points, larger values observed for some interferograms are related to the fact that the reconstruction quality varies from one point to another depending on its neighbors both in space and in time.

B. Miage Glacier

13 interferograms were produced from 14 consecutive acquisitions from December 2016 to March 2017. The quantity of gaps varies from 11.4 to 23.1 % and many interferograms are concerned with data gaps in the central part of the glacier. There are also three missing interferograms in the displacement time series. Note that the long and narrow shape of the glacier, in addition to discontinuities due to coherence loss, make the phase unwrapping challenging: 5 interferograms out of 13 are concerned with phase jumps during phase unwrapping. The correction of such phase jumps is difficult

since no other data set with similar spatial coverage and measurement accuracy is available.

Representative examples of the reconstruction are presented in Fig. 13. Case 1 (first row) contains 12.3% of data gaps, case 2 (second row) contains 18.6% of data gaps and case 3 (third row) contains 23.1% of data gaps. The estimated optimal number of EOF modes is 2. A global agreement is obtained between the reconstructed and the original interferograms. In case 1, the residual field is homogeneous but with the presence of clear discontinuities between segments of the glacier. This is due to phase jumps in the original interferogram because of coherence loss in the central part of the glacier. Time series of a point located in the discontinuity zone (P_2 , Fig. 13) and its reconstruction \hat{P}_2 are plotted in Fig. 12 (b), showing a similar behavior with errors falling within the range of nominal InSAR accuracy (<1cm). Note that most of the value shifts between P_2 and \hat{P}_2 are explained by unwrapping errors in the discontinuity zone at these dates (Fig 13).

In case 2, the displacement pattern is reconstructed with success, with some discontinuous values at the separation of the two terminal lobes, i.e. where most data gaps are observed in the time series. Reconstructed time series of a point located in this area (P_1) is also shown in Fig. 12 (b). Thanks to other interferograms where no phase jump is observed, EM-EOF reconstructs interferograms with phase jumps corrected. Case 3 presents a strongly degraded interferogram, with large quantities of data gaps and phase jumps. The reconstructed interferogram has a displacement pattern in accordance with other interferograms of good quality, although its amplitude seems slightly lower compared to the initial displacement field at the entry of the terminal lobes. The means and standard deviations of residuals of all interferograms are given in Table IV. The global observations are the same as in the case of the Gorner Glacier. In this case, the residuals are zero-centered for most interferograms (less than 0.01 cm in observed parts and less than 0.3 cm in cross-validation points). Moreover, the standard deviation values in this case are larger, which is mainly related to phase jumps and localized phase unwrapping errors. Besides the ability of gap filling, the EM-EOF method can also detect and correct displacement signal inconsistencies on individual interferograms in the time series.

C. Argentière Glacier

65 12-day interval displacement maps were generated using 66 Sentinel-1 A/B images between October 2016 and December 2017 using offset tracking.

The general quality of this data set is degraded compared to previous data sets because of very low SNR and strong correlated gaps in space and time. Due to the orientation of the glacier, the displacement is larger in the azimuth direction than in the LOS direction. Therefore, only the displacement time series in the azimuth direction is considered here. The quantity of gaps per displacement map varies from 2 % to almost 50 %. To show why this application is challenging, cross-RMSE $E(k)$ in function of the number of EOF modes k used in the reconstruction are displayed in Fig. 14. The minimum of $E(k)$ is found at $k = 58$ EOF modes, which

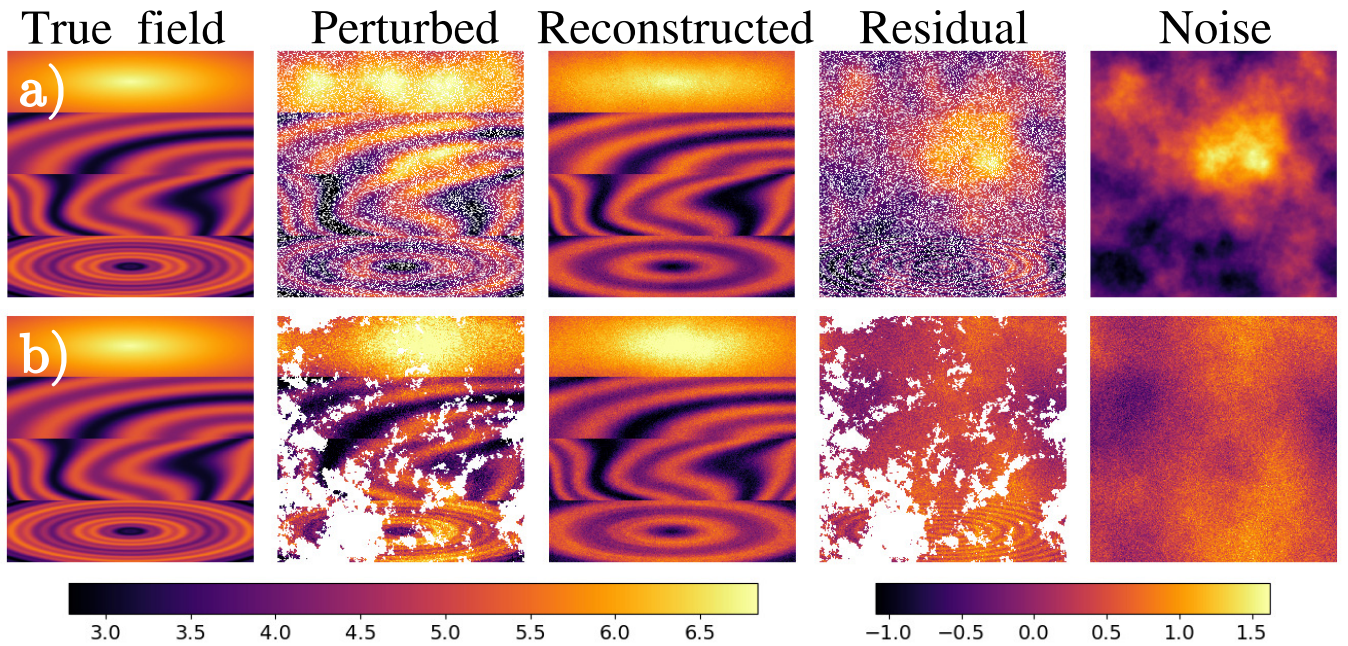


Fig. 7: Result of the reconstruction of a multiple pattern field [cm] perturbed by 30% of missing data and with SNR = 1.6. Top pattern is a linear field, middle patterns are three order fields (see Table I) and bottom pattern is a fourth order field. Displacement fields are perturbed by (a) random gaps and spatially correlated noise and (b) correlated gaps and spatio-temporally correlated noise. The residual is the difference between the reconstructed field and the perturbed field.

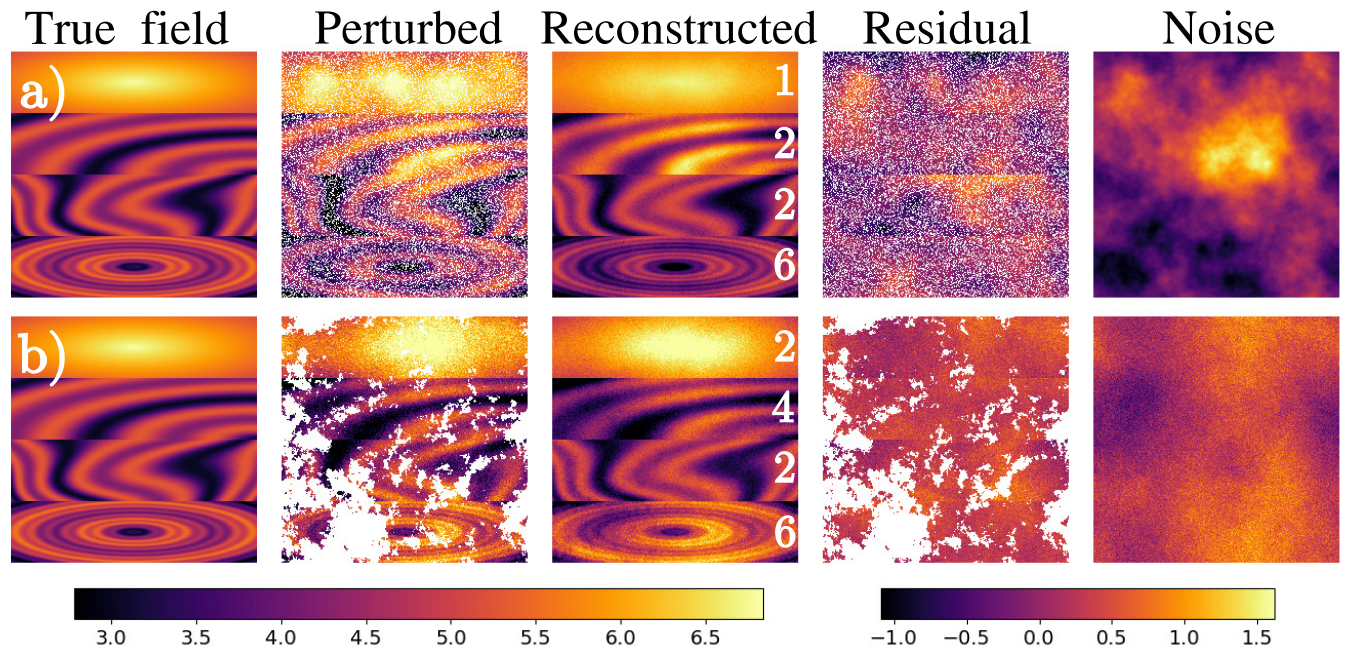


Fig. 8: Result of the 4 independent reconstructions of the multiple pattern fields [cm] showed in Fig. 7. Numbers are the estimated optimal number of EOF modes for each pattern. As in Fig. 7, displacement fields are perturbed by (a) random gaps and spatially correlated noise and (b) correlated gaps and spatio-temporally correlated noise.

	Gorner				Miage			
	Observed		Cross-validation		Observed		Cross-validation	
Date	Mean	σ	Mean	σ	Mean	σ	Mean	σ
2016/11/11-2016/11/17	0.028	0.741	0.114	1.043				
2016/11/17-2016/11/23	x	x	x	x				
2016/11/23-2016/11/29	0.089	0.951	0.046	1.724				
2016/11/29-2016/12/05	0.008	0.814	0.088	1.369	0.015	0.984	-0.134	0.974
2016/12/05-2016/12/11	0.048	0.808	-0.158	1.273	0.0008	1.068	-0.029	0.920
2016/12/11-2016/12/17	-0.005	0.662	0.057	1.191	0.002	0.720	-0.058	0.632
2016/12/17-2016/12/23	0.045	0.859	0.024	1.342	0.002	0.885	0.173	0.904
2016/12/23-2016/12/29	0.022	0.921	-0.072	1.419	-0.004	1.029	0.051	1.186
2016/12/29-2017/01/04	-0.048	0.721	-0.05	0.856	0.011	1.137	-0.056	0.773
2017/01/04-2017/01/10	0.0006	0.863	-0.022	1.108	0.001	0.837	0.016	0.825
2017/01/10-2017/01/16	x	x	x	x	x	x	x	x
2017/01/16-2017/01/22	-0.031	0.667	0.015	0.593	-0.0003	0.935	0.015	0.959
2017/01/22-2017/02/28	x	x	x	x	-0.002	1.396	-0.103	1.329
2017/01/28-2017/02/03	-0.034	0.869	0.09	0.968	-0.008	1.030	-0.083	1.039
2017/02/03-2017/02/09	-0.001	0.906	-0.083	1.518	x	x	x	x
2017/02/09-2017/02/15	-0.085	1.032	-0.219	1.782	0.003	1.091	-0.046	0.804
2017/02/15-2017/02/21	-0.011	0.884	-0.118	1.462	-0.009	1.042	0.232	1.029
2017/02/21-2017/02/27	-0.034	0.749	0.002	1.038	-0.032	1.070	-0.074	1.208
2017/02/27-2017/03/05	x	x	x	x	x	x	x	x
2017/03/05-2017/03/11	0.004	1.228	0.026	1.374				

TABLE IV: Mean (cm) and standard deviation σ (cm) of the residual fields on observed and cross-validation points over Gorner and Miage glaciers. The 'x' symbol refers to missing interferograms.

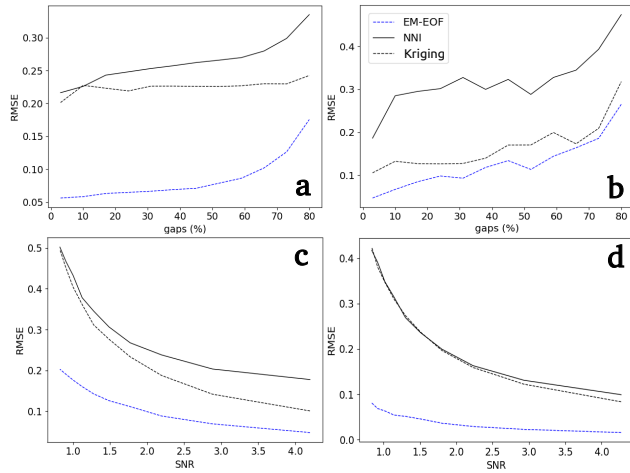


Fig. 9: Mean cross-RMSE [cm] of EM-EOF, NNI and Kriging in function of gaps quantity and SNR from 100 simulations. (a) random gaps, SNR = 2, spatially correlated noise, (b) correlated gaps, SNR = 2, spatially correlated noise, (c) spatially correlated noise, 30% missing data, random gaps, (d) spatio-temporally correlated noise, 30% missing data, random gaps.

is mainly due to strong mixing between displacement signal and noise. A large proportion of EOF modes are dominated by correlated noise and are interpreted as displacement signal, which makes the error decrease each time one EOF mode is added to the reconstruction. Results of the reconstructed displacements at three time intervals are presented in Fig. 15 with 20 EOF modes, which is the result after stage 2 and corresponds to a local minimum of $E(k)$ (after this minimum, the variation of the error is small). Cases 1, 2 and 3 (first, second and third lines) contain respectively 7.39%, 7.42% and 4.12% of data gaps. Reconstructed offsets show a global agreement with initial displacement fields. In missing data areas, reconstructed values can be sometimes questionable: in cases 2 and 3, reconstructed values in the bottom left and middle parts of the displacement field differ from the neighboring values and mark clear discontinuities. As shown in section III, the reconstruction quality depends more on SNR than on the quantity of gaps. Hence, discontinuities between missing data areas and neighboring areas are the result of low SNR since data gaps are not significant in this case (< 10%).

D. Comparison with NNI and Kriging

The performance of the EM-EOF in case of real data is assessed by comparing the reconstruction results with NNI/Kriging over the Gorner Glacier. In Miage and Argentière time series, large amount of phase jumps and low SNR do not allow for an objective comparison with NNI/Kriging which

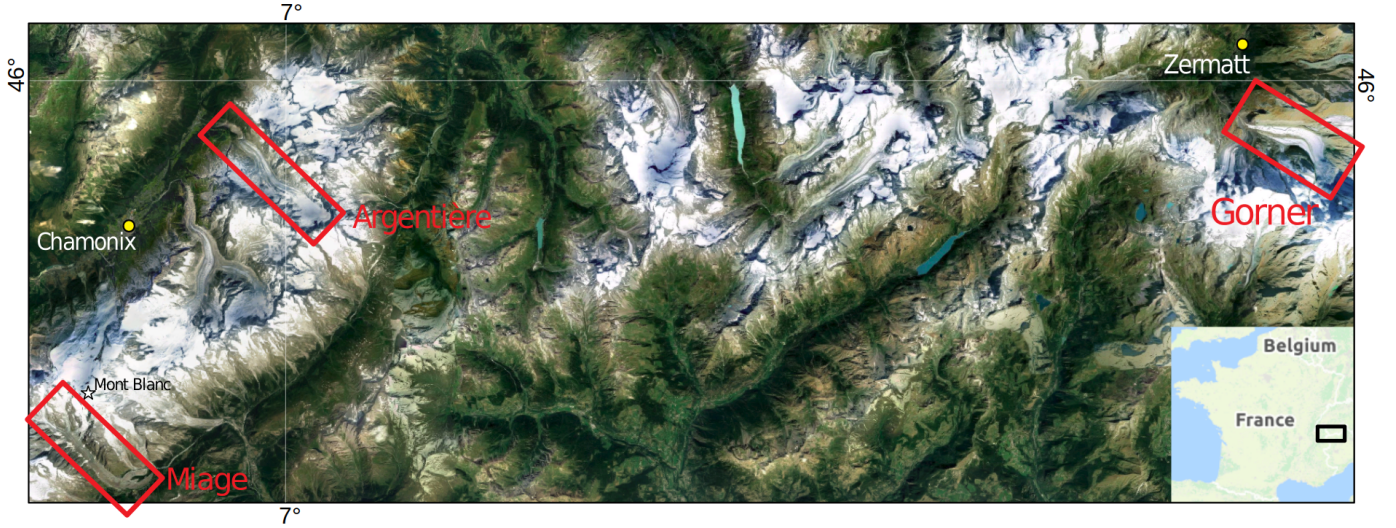


Fig. 10: Location of Gorner, Miage and Argentière glaciers. Gorner Glacier is located in the Valais, Swiss Alps, Miage and Argentière glaciers are located in the Mont-Blanc Massif, respectively in the Italian and French Alps.

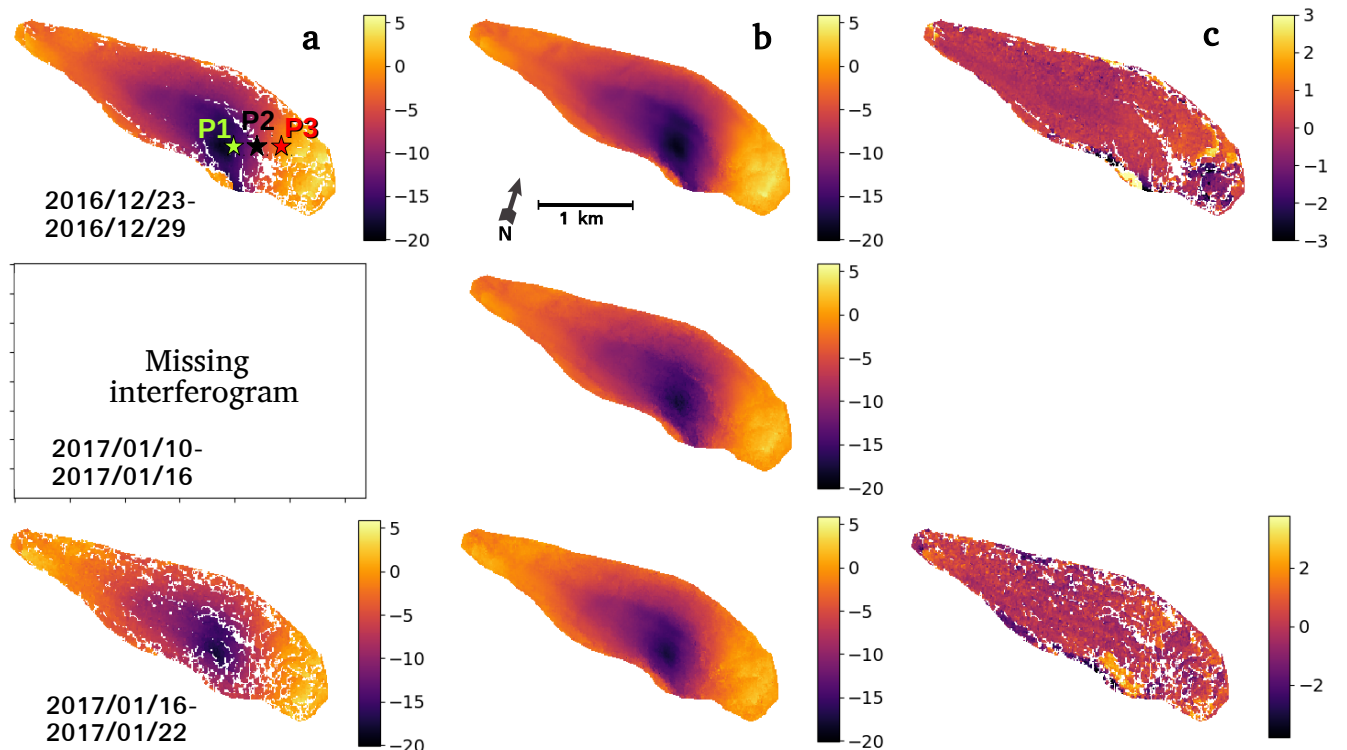


Fig. 11: a) Original, b) reconstructed interferograms and c) residuals (reconstruction-original) in radar geometry over the Gorner glacier at three time intervals (2016/12/23-2016/12/29, 2017/01/10-2017/01/16, 2017/01/16-2017/01/22). Time series of points at locations P₁, P₂ and P₃ are shown in Figure 12. Displayed values are in centimeters in the radar LOS.

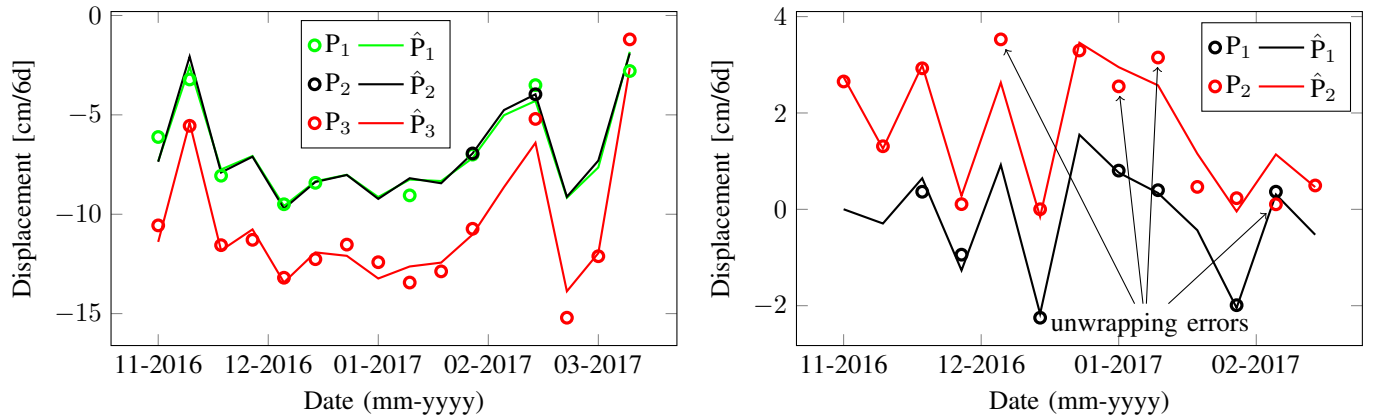


Fig. 12: Time series of displacement measurement in radar LOS over Gorner Glacier (left) and Miage Glacier (right) at different locations P₁, P₂ and P₃ (Fig. 11, Fig. 13) and their reconstructions \hat{P}_1 , \hat{P}_2 and \hat{P}_3 by the EM-EOF method. Circles represent existing values in the time series whereas lines are reconstructed values.

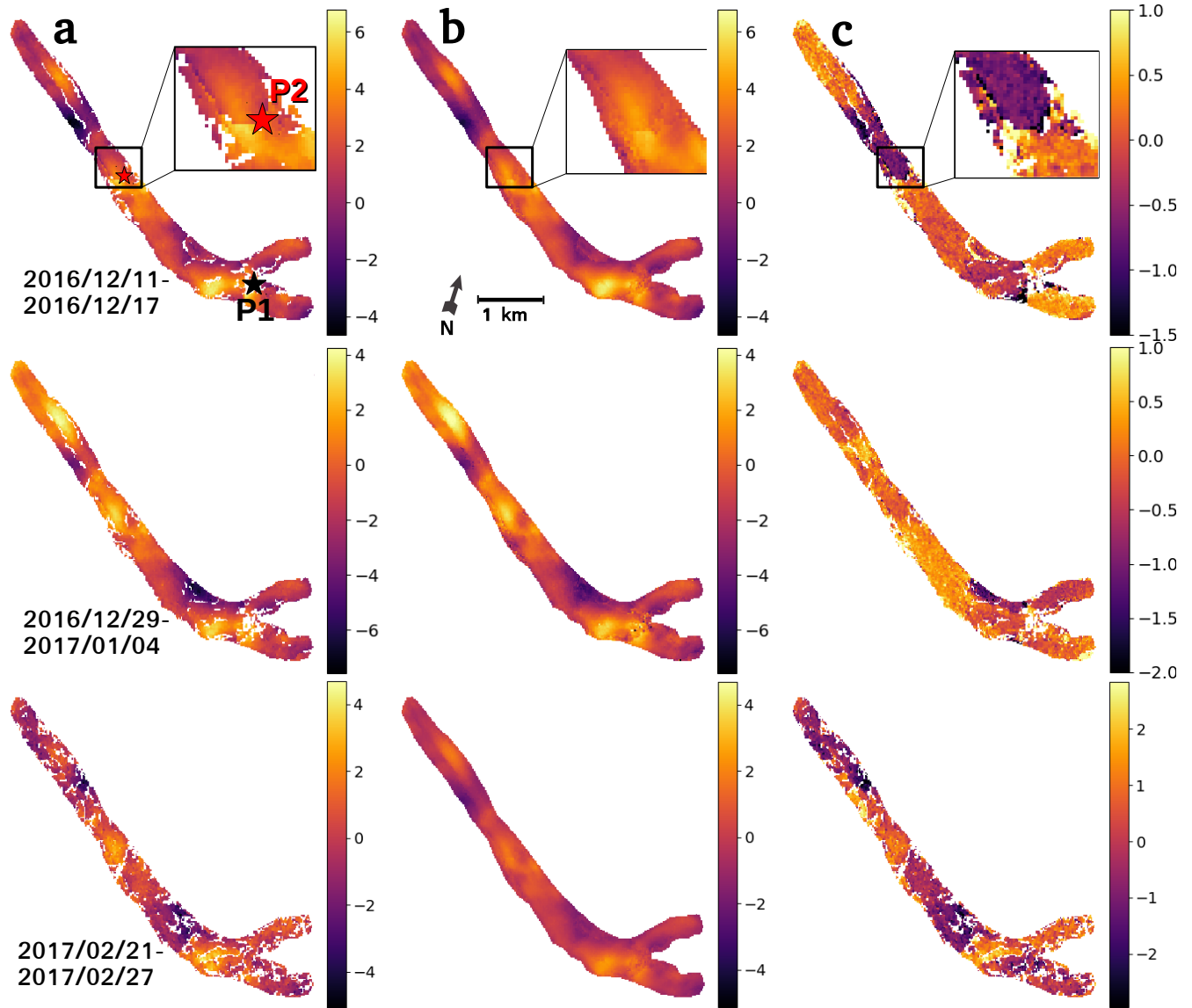


Fig. 13: a) Original, b) reconstructed interferogram and c) residual (reconstruction-original) in radar geometry over Miage glacier at three time intervals (2016/12/11-2016/12/17, 2016/12/29-2017/01/04 and 2017/02/21-2017/02/27). Temporal evolution of points at locations P₁ and P₂ are shown in Figure 12. Displayed values are in centimeters in the radar LOS.

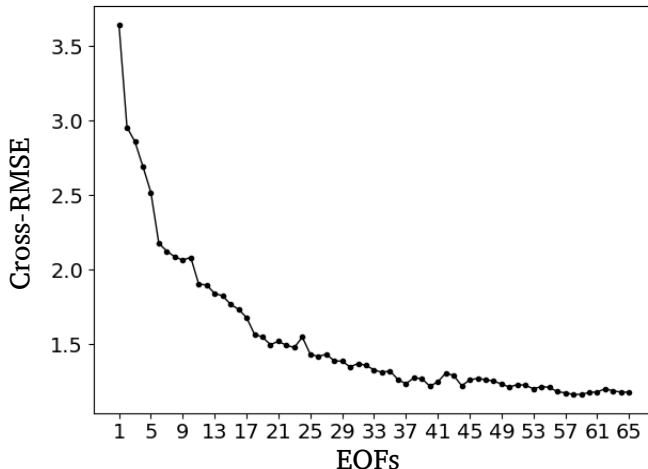


Fig. 14: Cross-RMSE $E(k)$ versus number of EOF modes k used in the reconstruction in case of the Argentière Glacier. The minimum of $E(k)$ is reached for $k = 58$ (stage 1). Result after stage 2 gives 20 EOF modes, which is a local minimum of $E(k)$.

are poorly adequate in these cases. Fig. 16 shows an example over interferogram 2017/01/16-2017/01/22. Note that due to Kriging extensive runtime, the comparison is performed on the top part of the glacier, where localized phase unwrapping errors and correlated data gaps exist. Similar conclusions are obtained as in synthetic simulations: the EM-EOF method provides significant better interpolation compared to NNI/Kriging, especially in areas with correlated data gaps and phase jumps where smoother and consistent reconstruction is obtained.

V. CONCLUSION

EM-EOF is a 2-stage iterative method based on the eigenvalue decomposition of the temporal covariance to retrieve missing values in time series of SAR-derived displacement measurement. After an initial filling of the missing values by the spatial mean, this method finds the optimal number of EOF modes to reconstruct the incomplete time series using adaptive cross-validation. Then, it proceeds to an update of the missing values until the convergence of the cross-RMSE is reached.

Synthetic simulations with a thorough error analysis have been carried out to show the efficiency of the method and to determine its sensitivity to the complexity of the displacement signal, the type of noise, SNR, the quantity and the type of gaps. It has been shown that EM-EOF is more sensitive to noise than gaps, except with large quantities of random data gaps which can significantly affect the quality of the reconstruction. When noise is spatio-temporally correlated, the optimal number of EOF modes can be over-estimated because of the difficulty in separating displacement signal and noise due to similar behaviors.

Real data applications confirm the efficiency of the EM-EOF method, with the possibility to handle challenging missing data cases as complete missing interferograms, correlated data gaps, low SNR and phase jumps. In this way, the EM-EOF method can help to increase the effective size of the

time series, and can thus facilitate the understanding of the phenomenon under observation, particularly when data gaps in displacement time series is a frequent issue. The last application over the Argentière Glacier shows a limiting condition on the data (low SNR) for EM-EOF to be fully operative, that is when the displacement signal is strongly contaminated with noise induced here by the computation uncertainties of surface velocities due to low spatial resolution (22 m in the azimuth direction in interferometric mode) and insufficiently large displacement.

Future works will include 1) estimating a spatio-temporal covariance matrix [23], [40] instead of a temporal covariance matrix in order to better characterize propagating spatio-temporal structures in the signal and 2) apply EM-EOF to complex interferogram time series, i.e. reconstruct missing values before phase unwrapping to improve low SNR and discontinuities issues in order to facilitate phase unwrapping.

VI. ACKNOWLEDGMENTS

This work has been supported by the Programme National de Télédétection Spatiale (PNTS, <http://www.insu.cnrs.fr/pnts>), grant PNTS-2019-11, and by the SIRGA projet funded by Université Savoie Mont Blanc.

APPENDIX

SYNTHETIC CONSTRUCTION OF SPATIALLY AND SPATIO-TEMPORALLY CORRELATED NOISE

Spatially correlated noise is generated using an auto-correlation function of the form $c(z) = z^{-\gamma}$, where the variation of parameter γ allows to tune the correlation distance. The value of $c(z)$ represents the degree of correlation of two points distant from z . This function is then used to filter and modulate a white Gaussian noise in the Fourier domain.

Spatio-temporally correlated noise is the sum of a spatially correlated noise and a temporally correlated noise. The former is generated as previously described, and the latter is formed using a Cholesky decomposition of a positive semi-definite temporal covariance matrix \mathbf{R} which verifies:

$$\mathbb{E}[\mathcal{Z}\mathcal{Z}^T] = \mathbf{R} \quad (11)$$

where $\mathcal{Z} \in \mathbb{R}^{n \times p}$ is the desired correlated noise and $\mathbb{E}[\cdot]$ denotes the expectation operator. The elements of matrix \mathbf{R} at position (i, j) are given by:

$$(r_{ij})_{1 \leq i \leq n, 1 \leq j \leq n} = \rho^{|i-j|} \quad (12)$$

where parameter ρ falls in the $[0, 1]$ interval and acts as a tuner of the time correlation: a value of 0 means that the simulated noise is not correlated in time, whereas a value close to 1 means that the noise is fully correlated in time. Matrix \mathbf{R} is positive semi-definite, which allows us to apply a Cholesky decomposition:

$$\mathbf{R} = \mathbf{L}\mathbf{L}^T \quad (13)$$

where \mathbf{L} and its transpose \mathbf{L}^T are respectively low and high triangular matrices. A random $n \times p$ matrix \mathbf{Y} following a normal distribution is generated to resolve:

$$\mathcal{Z} = \mathbf{LY} \quad (14)$$

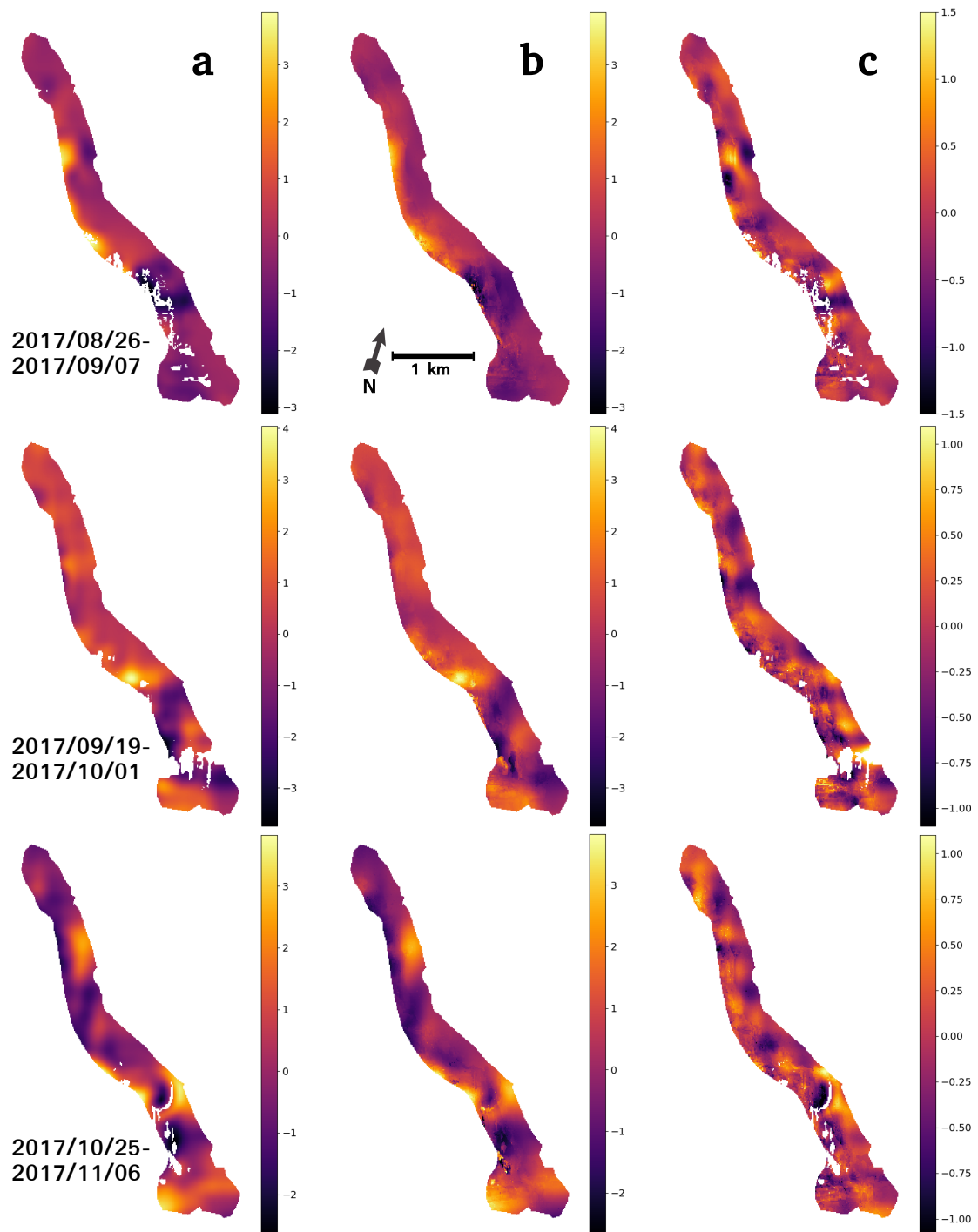


Fig. 15: a) Original, b) reconstructed offset map and c) residual (reconstruction-original) in radar geometry over the Argentière glacier at three time intervals (2017/08/26-2017/09/07, 2017/09/19-2017/10/01 and 2017/10/25-2017/11/06). Displayed values are in meters in the azimuth direction.

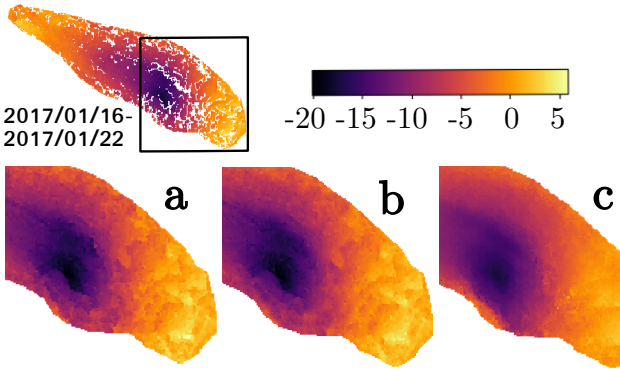


Fig. 16: Reconstructed interferogram [cm] (2017/01/16–2017/01/22) over Gorner Glacier using a) NNI, b) Kriging and c) EM-EOF methods.

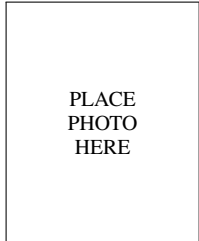
\mathcal{Z} is a $n \times p$ matrix where the degree of correlation between each line is directly tuned by parameter ρ in Eq. (12). To show that \mathcal{Z} has the desired temporal covariance \mathbf{R} as in (11):

$$\mathbb{E}[\mathcal{Z}\mathcal{Z}^T] = \mathbf{L}\mathbb{E}[\mathbf{Y}\mathbf{Y}^T]\mathbf{L}^T = \mathbf{R} \quad (15)$$

REFERENCES

- [1] Y. Yan, A. Dehecq, E. Trouve, G. Mauris, N. Gourmelen, and F. Vernier, “Fusion of remotely sensed displacement measurements: Current status and challenges,” *IEEE Geoscience and Remote Sensing Magazine*, vol. 4, no. 1, pp. 6–25, 2016.
- [2] D. B. Rubin, “Inference and missing data,” *Biometrika*, vol. 63, no. 3, pp. 581–592, 1976.
- [3] R. J. A. Little and D. B. Rubin, *Statistical analysis with Missing Data*. New York: Wiley, 1987.
- [4] R. W. Preisendorfer, *Principal Component Analysis in Meteorology and Oceanography*. Elsevier, 1988.
- [5] F. Melgani, “Contextual Reconstruction of Cloud-Contaminated Multitemporal Multispectral Images,” *IEEE Trans. Geosci. Remote Sens.*, vol. 44, pp. 442–455, Feb. 2006.
- [6] C.-H. Lin, K.-H. Lai, Z.-B. Chen, and J.-Y. Chen, “Patch-based information reconstruction of cloud-contaminated multitemporal images,” *IEEE Trans. Geosci. Remote Sens.*, vol. 52, no. 1, pp. 163–174, 2014.
- [7] W. Wu, L. Ge, J. Luo, R. Huan, and Y. Yan, “A spectral-temporal patch-based missing area reconstruction for time-series images,” *Remote Sensing*, vol. 10, p. 1560, 2018.
- [8] Q. Zhang, Q. Yuan, C. Zeng, X. Li, and Y. Wei, “Missing data reconstruction in remote sensing image with a unified spatial-temporal-spectral deep convolutional neural network,” *IEEE Transactions on Geoscience and Remote Sensing*, vol. 56, no. 8, pp. 4274–4288, Aug 2018.
- [9] J. M. Beckers and M. Rixen, “EOF calculations and data filling from incomplete oceanographic datasets,” *J. Atmos. Oceanic Technol.*, vol. 20(12), pp. 1836–1856, 2003.
- [10] D. Kondrashov and M. Ghil, “Spatio-temporal filling of missing points in geophysical data sets,” *Nonlinear Processes Geophys.*, vol. 13, pp. 151–159, 2006.
- [11] A. Alvera-Azcarate, A. Barth, J.-M. Beckers, and R. H. Weisberg, “Multivariate reconstruction of missing data in sea surface temperature, chlorophyll, and wind satellite fields,” *J. Geophys. Res.*, vol. 112, no. C03008, 2007.
- [12] K. Hocke and N. Kämpfer, “Gap filling and noise reduction of unevenly sampled data by means of the Lomb-scargle periodogram,” *Atmospheric Chemistry and Physics*, vol. 9, no. 12, pp. 4197–4206, 2009. [Online]. Available: <https://www.atmos-chem-phys.net/9/4197/2009/>
- [13] A. Verger, F. Baret, M. Weiss, S. Kandasamy, and E. Vermote, “The cacao method for smoothing, gap filling and characterizing seasonal anomalies in satellite time series,” *IEEE Transaction on Geoscience and Remote Sensing*, vol. 51, no. 4, pp. 1963–1972, 2013.
- [14] F. Gerber, R. de Jong, M. E. Schaepman, G. Schaeppman-Strub, and R. Furrer, “Predicting missing values in spatio-temporal remote sensing data,” *IEEE Trans. Geosci. Remote Sens.*, vol. 56, no. 5, pp. 2841–2853, 2018.
- [15] S. Gudmundsson, F. Sigmundsson, and J. Carstensen, “Three-dimensional surface motion maps estimated from combined interferometric synthetic aperture radar and GPS data,” *Journal of Geophysical Research*, vol. 107, 10 2002.
- [16] R. Jolivet, R. Grandin, C. Lasserre, M.-P. Doin, and G. Peltzer, “Systematic InSAR tropospheric phase delay corrections from global meteorological reanalysis data,” *Geophysical Research Letters*, vol. 38, no. 17, 2011.
- [17] M.-C. Wu, J. G. Liu, and P. J. Mason, “Adaptive local kriging to retrieve slant-range surface motion maps of the wenchuan earthquake,” *International Journal of Remote Sensing*, vol. 34, no. 21, pp. 7589–7606, 2013.
- [18] W.-Y. Chang, M.-C. Wu, Y.-L. Chang, S.-Y. Shih, and B. Huang, “Gpu acceleration of adaptive local kriging applied to retrieving slant-range surface motion maps,” *IEEE J. Sel. Top. Appl. Earth Obs. Remote Sens.*, vol. 11, no. 11, pp. 4317–4325, 2018.
- [19] N. Choudhury, A. Rahman, and S. Ferdousi, “Kriging infill of missing data and temporal analysis of rainfall in north central region of bangladesh,” *J. Climatol. Weather Forecasting*, vol. 3, no. 141, 2015.
- [20] H. Shen, X. Li, Q. Chen, C. Zeng, G. Yang, H. Li, and L. Zhang, “Missing information reconstruction of remote sensing data: A technical review,” *IEEE Geosci. Remote Sens. Mag.*, vol. 3, pp. 61–85, 09 2015.
- [21] M. Lepot, J.-B. Aubin, and F. H. Clemens, “Interpolation in time series: An introductory overview of existing methods, their performance criteria and uncertainty assessment.” *Water*, vol. 9, no. 796, 2017.
- [22] C. Xu, “Reconstruction of gappy GPS coordinate time series using empirical orthogonal functions,” *J. Geophys. Res. Solid Earth*, vol. 121, pp. 9020–9033, 2016.
- [23] M. Ghil, M. Allen, M. D. Dettinger, K. Ide, D. Kondrashov, M. Mann, A. Robertson, A. Saunders, Y. Tian, F. Varadi, and P. Yiou, “Advanced spectral methods for climatic time series.” *Review of Geophysics*, vol. 40, 1, pp. 1–41, 2002.
- [24] A. Hannachi, I. Jolliffe, and D. Stephenson, “Empirical orthogonal functions and related techniques in atmospheric science: A review.” *Int. J. Climatol.*, vol. 27, pp. 1119–1152, 2007.
- [25] R. Prébet, Y. Yan, M. Jauvin, and E. Trouvé, “A data-adaptive eof based method for displacement signal retrieval from insar displacement measurement time series for decorrelating targets,” *IEEE Trans. Geosci. Remote Sens.*, vol. 57, no. 8, pp. 5829–5852, 2019.
- [26] A. P. Dempster, N. M. Laird, and D. B. Rubin, “Maximum likelihood from incomplete data via the em algorithm,” *J. Royal Statistical Society. Series B (Methodological)*, vol. 39, no. 1, pp. 1–38, 1977.
- [27] J.-M. Brankart and P. Brasseur, “Optimal analysis of in situ data in the western Mediterranean using statistics and cross-validation,” *J. Atmos. Oceanic Technol.*, vol. 13, pp. 477–491, 1995.
- [28] A. P. Kositsky and J.-P. Avouac, “Inverting geodetic time series with a principal component analysis-based inversion method.” *J. Geophys. Res.*, vol. 115, no. B03401, 2010.
- [29] W. C. Thacker, “Metric-based principal components: data uncertainties,” *Tellus A*, vol. 48, no. 4, pp. 584–592, 1996.
- [30] G. R. North, T. L. Bell, R. F. Cahalan, and F. J. Moeng, “Sampling errors in the estimation of empirical orthogonal functions,” *Monthly Weather Review*, vol. 110, no. 7, pp. 699–706, 1982.
- [31] J. Overland and R. W. Preisendorfer, “A significance test for principal components applied to a cyclone climatology,” *Monthly Weather Review*, vol. 110, p. 1, 01 1982.
- [32] H. Björnsson and S. A. Venegas, *A Manual for EOF and SVD Analyses of Climatic Data*, Department of Atmospheric and Oceanic Sciences and Center for Climate and Global Change Research. McGill University, 02 1997.
- [33] K. Lounici, “High-dimensional covariance matrix estimation with missing observations,” *Bernoulli*, vol. 20, no. 3, pp. 1029–1058, 08 2014. [Online]. Available: <https://doi.org/10.3150/12-BEJ487>
- [34] T. T. Cai and A. Zhang, “Minimax rate-optimal estimation of high-dimensional covariance matrices with incomplete data,” *Journal of Multivariate Analysis*, vol. 150, pp. 55 – 74, 2016. [Online]. Available: <http://www.sciencedirect.com/science/article/pii/S0047259X16300239>
- [35] T. Schneider, “Analysis of incomplete climate data: Estimation of mean values and covariance matrices and imputation of missing values,” *J. Climate*, vol. 14, pp. 853–871, 2001.
- [36] S. Heimann, M. Kriegerowski, M. Isken, S. Cesca, S. Daout, F. Grigoli, C. Juretzek, T. Megies, N. Nooshiri, A. Steinberg, H. Sudhaus, H. Vasyura-Bathke, T. Willey, and T. Dahm, “Pyrocko - an open-source seismology toolbox and library. v. 0.3,” *GFZ Data Services*, 2017.
- [37] R. Sibson, Ed., *A brief description of natural neighbor interpolation*, no. 24–27. Sheffield, UK: Proceedings of the Interpreting Multivariate Data, Mar. 1980.

- [38] D. R. Jones, “A taxonomy of global optimization methods based on response surfaces,” *J. Global Optim.*, vol. 21, no. 4, pp. 345–383, Dec 2001. [Online]. Available: <https://doi.org/10.1023/A:1012771025575>
- [39] M. Gentile, F. Courbin, and G. Meylan, “Interpolating point spread function anisotropy,” *Astron. Astrophys.*, vol. 549, p. A1, Dec 2012. [Online]. Available: <http://dx.doi.org/10.1051/0004-6361/201219739>
- [40] R. Vautard, P. You, and M. Ghil, “Singular spectrum analysis: a toolkit for short, noisy chaotic signals,” *Physica D*, vol. 58, pp. 95–126, 1992.



Alexandre Hippert-Ferrer Biography text here

PLACE
PHOTO
HERE



Yajing Yan Biography text here

PLACE
PHOTO
HERE



Philippe Bolon Biography text here.

PLACE
PHOTO
HERE